

AN EVALUATION OF THE CARBURISED MICROSTRUCTURE OF FERRITIC 9Cr-1Mo STEEL FOLLOWING EXPOSURE TO HOT CO₂ GAS

C. Liu¹, P.J. Heard¹, O.D. Payton¹, L. Picco¹, I. Griffiths¹ and P.E.J. Flewitt^{1,2}

¹ Interface Analysis Centre, HH Wills Physics Laboratory, University of Bristol, Bristol, BS8 1TL, UK

² HH Wills Physics Laboratory, University of Bristol, Bristol, BS8 1TL, UK

ABSTRACT

When finned experimental tubing samples of 9Cr-1Mo ferritic steel were exposed for extended periods to hot CO₂ containing traces of CO, H₂, H₂O and CH₄, they were subject to a combination of oxidation and carburisation. The microstructure of the bulk material was examined to establish the underlying mechanisms of carburisation. Selected experimental samples were exposed to the simulated gas at temperatures of 580 °C for 2546 hrs. To underpin the factors that influence carburisation the morphology, composition and area fraction of carbide precipitates were evaluated using focused ion beam imaging, high-speed atomic force microscopy and scanning transmission electron microscopy techniques. The results are discussed in relation to the underlying carburisation mechanism.

INTRODUCTION

In many industries a range of medium chromium ferritic – martensitic steels are used for structural components required for high temperature service^[1]. For example, 9Cr1Mo ferritic steel is adopted for components used in advance gas-cooled nuclear reactors (AGR) that are in service in the UK. These components are subject to temperatures in the range 350 °C to around 480 °C^[2,3], and operate in an environment of hot carbon dioxide gas. As a consequence the material can be subject to both oxidation and carburisation^[4]. Consideration of the life extension of these reactors has revived interest in this material^[5]. The overall reaction leading to degradation of 9Cr-1Mo steel by the coolant gas can be described in two stages according to the following reactions:



Where M represents Fe and Cr. The reaction between metal and oxidant produces oxide consisting of (Fe_xCr_{3-x}O₄)^[6-8]. Carbon diffuses inward resulting in carburisation of the metal matrix and producing carbides that may vary from (Fe,Cr)₃C to (Fe,Cr)₇C₃ and (Fe,Cr)₂₃C₆ etc.^[9-12]. Equations (1) and (2) represent the process of oxidation and carburisation respectively. In this paper we explore the morphology, distribution and chemical composition of carbide precipitates analysed with different techniques. The results are discussed with respect to the inter-relation between these three parameters and the carburisation process.

EXPERIMENTAL

An experimental ferritic 9Cr-1Mo steel sample was analysed to study the carburisation mechanisms by oxidation in an autoclave with flowing simulant coolant gas, consisting primarily of CO₂ with traces of CO, H₂, H₂O and CH₄ at 580 °C for 2546 hrs. The chemical composition of the sample before exposure is shown in Table 1.

Table 1: Chemical composition (in wt. %) of samples before exposure.

Element	C	S	Si	Mg	P	Cr	Mo	Ni	Co	Cu	Fe
Weight %	0.093	0.008	0.67	0.47	0.011	9.20	1.04	0.21	0.02	0.16	Bal.

Prior to examination, the sample was mechanically polished using a range of SiC abrasive papers and diamond pastes followed by vibro-polishing with colloidal silica suspension to obtain a finely polished surface suitable for optical microscopy (OM), focused ion beam imaging (FIB) and high speed atomic force microscopy (HS-AFM). The composition of the carbide precipitates and the surrounding area was established using scanning transmission electron microscopy (STEM) with energy dispersive spectroscopy (EDS) analysis. For HS-AFM analysis, high quality sample surface preparation is required to ensure a clean and flat surface. A suitable protocol has been described previously^[13].

HS-AFM images were acquired using a Bristol Nano Dynamics Ltd system which is capable of imaging at up to 2 Megapixels per second. High -speed AFM was used to cover significantly larger areas than can be mapped using a conventional AFM in a fraction of the time. Carbides and other features are identified by their height following sample polishing and utilising the difference in carbide hardness compared with the parent material to leave them proud of the surface^[14]. Custom software was used to extract the carbide precipitate features and characterise them according to their area, height and aspect ratio. The carbide area fraction as a function of position across the middle part of the central fin in Figure 1a was generated by acquiring a series of HS-AFM images of $4.5 \times 4.5 \mu\text{m}$ in size. Twenty such images were obtained and the carbide area fractions plotted as a function of position from the centre of the fin to the metal/oxide interface. To characterise the carbide coverage further, a sparse matrix of images, each of $4.5 \times 1.5 \mu\text{m}$ in size and spaced at $25 \mu\text{m}$ intervals were obtained, covering the entire right hand side of the central fin. Carbide area fractions were extracted from these and colour coded to indicate the area fraction as a function of position. Finally, a set of 1600 overlapping HS-AFM images were obtained from an area close to the metal-oxide interface (shown in Figure 1b) and stitched together to provide a large area high-resolution image for comparison with the FIB results.

The focused ion beam instrument used for this work was an FEI FIB-201 single gallium ion beam instrument, operating at 30keV beam energy. FIB images were obtained by initially cleaning regions of the sample by sputtering an area of $120 \times 100 \mu\text{m}$ at 11nA beam current for about 10s to remove surface contamination and oxide. Ion-induced secondary electron images were then obtained at 150 or 90pA beam current showing topographical and ion channelling contrast. Following the acquisition of the initial image, XeF_2 gas was introduced into the system for a few seconds to functionalise the surface, and further images were obtained at low and high magnification. The resulting images have reduced ion channelling contrast, but show carbide precipitates as darker regions. The centre fin of the sample was analysed by FIB imaging following three horizontal paths at 500, 1000 and $1500 \mu\text{m}$ from the fin tip as shown in Figure 1a. Five sets of images were obtained at each height, and the carbide area fractions were obtained using standard image processing software to threshold the images according to greyscale and count pixels. A further set of images was obtained from the tip of the fin travelling down through the centre of the fin. The image used for comparison with HS-AFM was obtained in the same way.

A thin foil of $15 \times 6 \times 0.1 \mu\text{m}$ was prepared using the ion milling, lift out method in a FEI Helios NanoLab 600i combined FIB/SEM system. The foil was analysed in the STEM mode using an Oxford Instruments AztecTEM advanced EDS system with X-Max 80 detector.

RESULTS

An optical micrograph of the polished specimen is shown in Figure 1a, while a FIB image of the central fin is shown in Figure 1b. The marked area in Figure 1b shows a region that was analysed with both HS-AFM and FIB imaging at high resolution for direct comparison. Figure 2 shows images of the region marked in Figure 1b. A focused ion beam induced secondary electron image after surface cleaning producing channelling contrast is shown in Figure 2a. The corresponding image after exposure to XeF_2 gas is shown in Figure 2b.

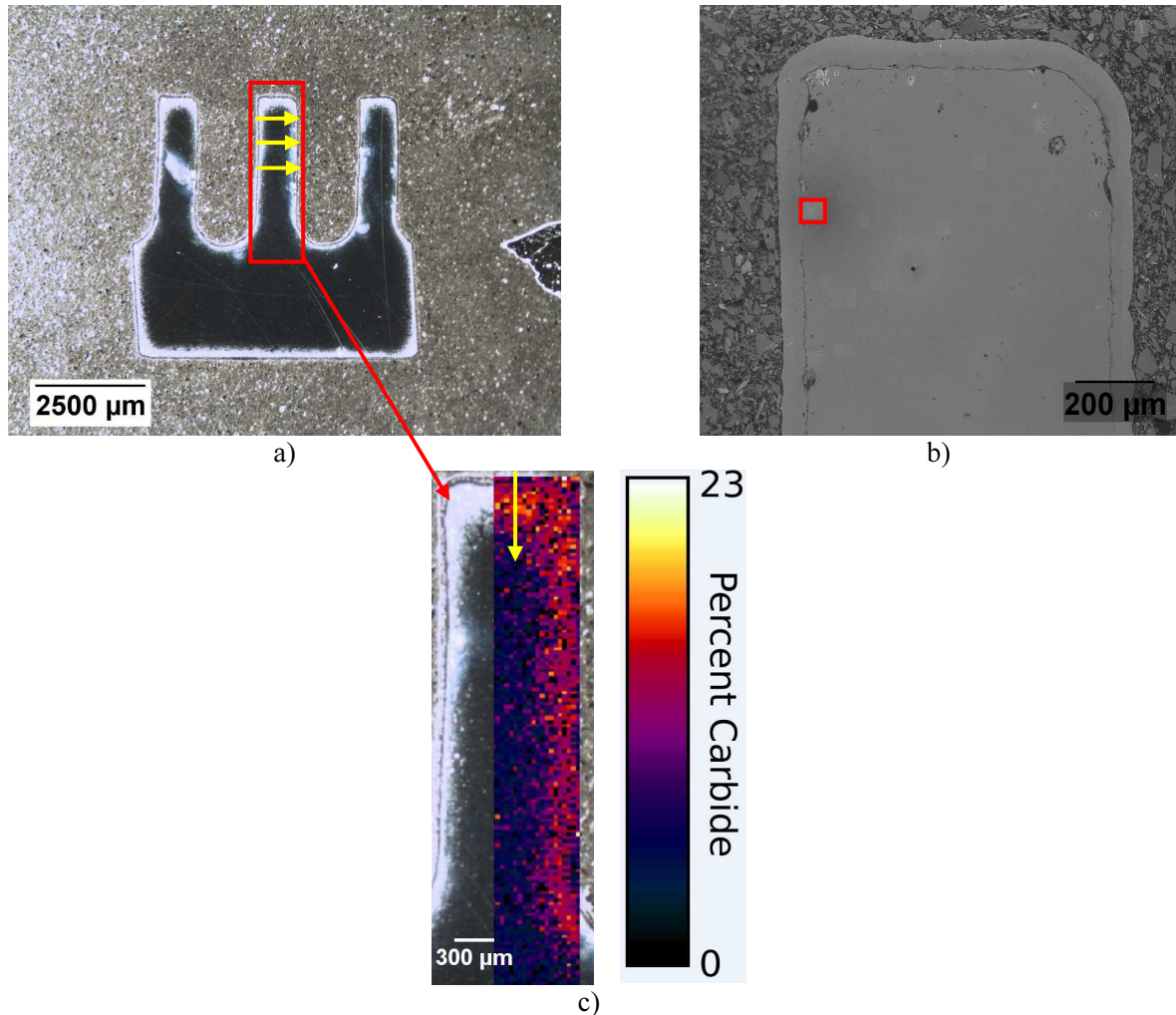


Figure 1: a) Optical image of the prepared specimen. b) FIB image of the middle fin showing an area analysed using HS-AFM and FIB imaging. c) Optical image of middle fin overlaid with HS-AFM map of measured carbide percentage using thresholding software on a sparse data set of frames.

The channelling contrast is now suppressed and the carbides are visible as darker regions in the image. It is evident that larger carbides are present at the grain boundaries, together with smaller intragranular carbide precipitates. A section of the same image at higher magnification is displayed in Figure 2c, together with the corresponding HS-AFM image in Figure 2d. Clearly the XeF₂/FIB image and the HS-AFM image are in general agreement regarding the morphology and distribution of carbides which are shown as dark areas in the FIB image and as brighter raised areas in the HS-AFM image. The larger carbides at the grain boundaries are assumed to be M₂₃C₆, and both FIB and HS-AFM images show a similar distribution. The smaller needle-like intragranular carbide distribution is also in general agreement between the two images, although there are small differences at high magnification. The reason for this is not clear but will be further investigated. The HS-AFM image reveals additional height changes from grain to grain.

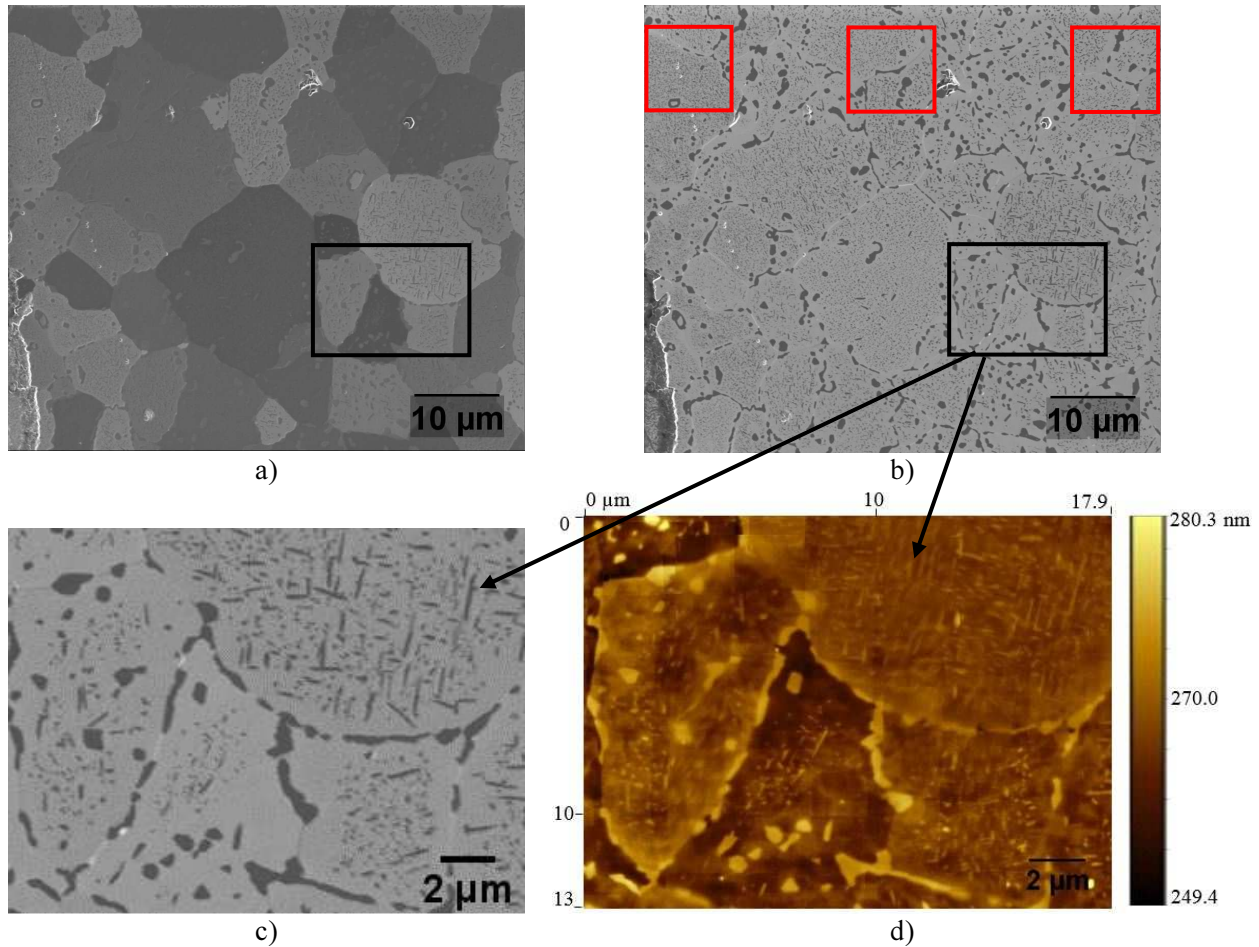


Figure 2: a) Initial FIB micrograph of the area marked in Figure 1b. b) The corresponding XeF₂ FIB image. c) Detailed XeF₂ FIB image; d) Composite HS-AFM image from same area showing 31 nm height range.

Thresholding was used to obtain carbide area fraction from both FIB and HS-AFM images. The results are presented in Figure 3. FIB images were obtained along the direction of the arrows shown in Figure 1a and from the fin tip downwards through the middle of the fin as shown in Figure 1c. Figure 3 shows that the carbide area fraction at the edge of the fin is higher than that at the fin centre. However, there are small differences between the three profiles at different distances from the fin tip. A carbide area fraction map of the right-hand side of the middle fin obtained from sparse HS-AFM images is shown in Figure 1c. The map shows that most carbides are distributed in the region about 200 μm from the fin side and 570 μm from the fin tip. As described in the experimental section, the area fraction from the FIB images was extracted from an area $120 \times 100 \mu\text{m}$ while for the HS-AFM images extracts were obtained from an area $4.5 \times 1.5 \mu\text{m}$. The plots from the HS-AFM measurements therefore have more spatial detail, and show that the carbide area fraction in the area next to the oxide is lower than that obtained from the FIB, which can be also observed from Figure 3b. An area of $10 \times 10 \mu\text{m}$ from the same region in Figure 2b was processed at locations 5 μm , 30 μm and 55 μm from the metal/oxide interface (red squares marked in Figure 2b), with image processing software to extract the area percentage and average size of the fine needle-shape carbides and coarse carbides respectively in Table 2. These data indicate that there is a lower carbide area fraction next to the oxide from HS-AFM. Clearly the total area percentage of carbide precipitates, including both fine and coarse carbide precipitates, increases with increasing distance to the metal/oxide interface in the region examined, and the size of both carbides increases with

increasing distance to the interface. Table 2 indicates a lower area percentage of coarse carbides in the area 5 μm from interface, which is the main reason for the lower carbide area fraction on the edge of the fin from HS-AFM results. A similar trend is generally observed between the plots from FIB and HS-AFM in Figure 3a.

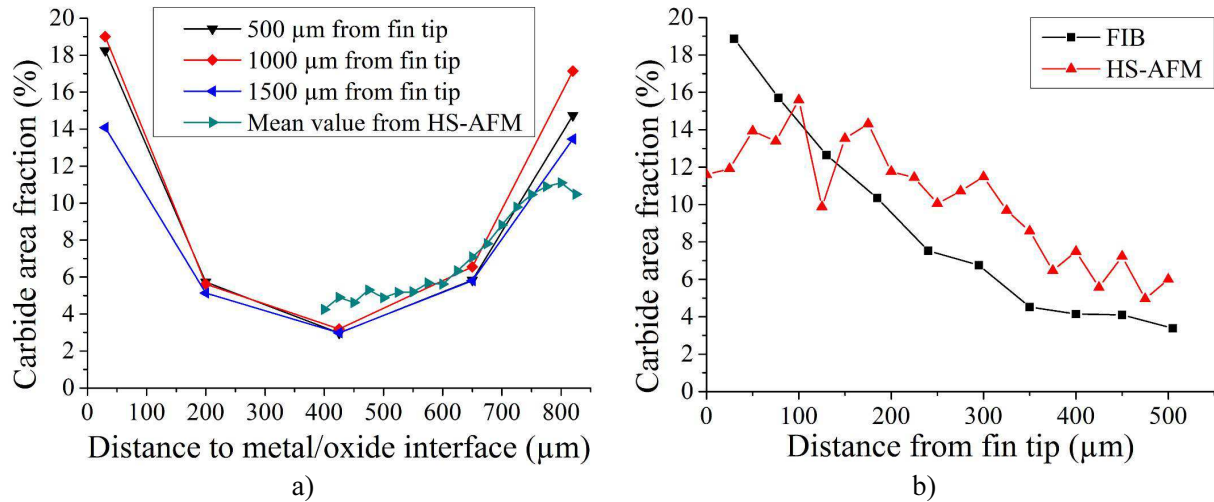


Figure 3: Carbide area fraction from both FIB and HS-AFM images against distance from metal/oxide interface a) across the fin; b) From the fin tip downwards through the centre of the fin.

Table 2: The area percentage and average size of two types of carbide from different locations

	5 μm from interface		30 μm from interface		55 μm from interface	
	Area %	Average size (μm^2)	Area %	Average size (μm^2)	Area %	Average size (μm^2)
Fine carbides	6.4	0.01	5.1	0.01	6.5	0.02
Coarse carbides	5.1	0.23	8.3	0.23	8.7	0.26

From the FIB and HS-AFM images, it appears that there are fewer coarse carbides but more small needle-shaped carbide precipitates present in the regions close to the oxide. The coarse carbides are observed both at grain boundaries and within the grains while small needles are found to be only intragranular. Since the carbides exist with two morphologies thin foil samples of these features were extracted using standard FIB lift-out techniques and examined using STEM, Figure 4. As shown in Figure 4a and c respectively, the STEM images show differences between these two types of carbides. EDS line scans were used for chemical composition analysis; their locations are shown in Figure 4a and 4c. The cross-section of a small needle was selected to minimise any contribution from the matrix. EDS results of the examined small needle and coarse carbide are shown in Figure 4b and d respectively. The chemical composition of the small needles and coarse carbides are different. The small needle exhibits very high Cr concentration (50-90 wt. %) but very low Fe (less than 5 wt. %), whereas the Cr and Fe concentrations in the coarse carbide are around 50 and 30 wt. % respectively.

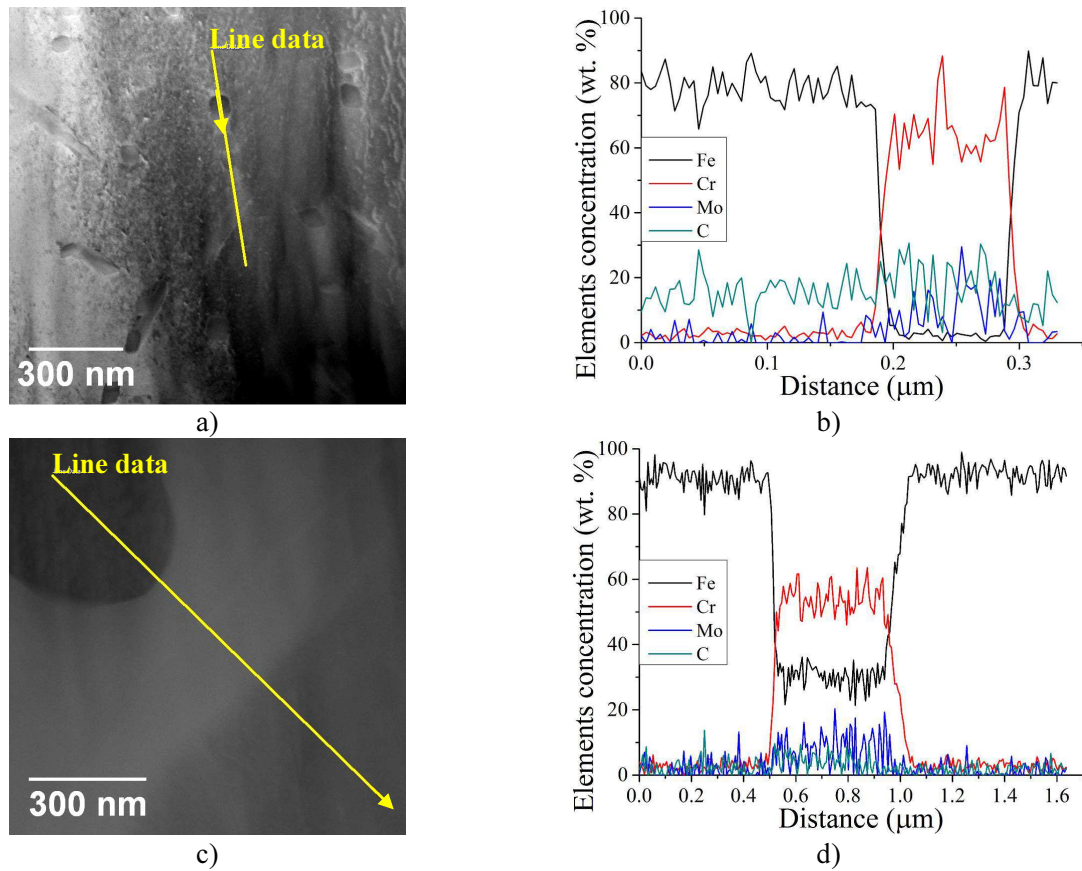


Figure 4: a) STEM image of needle carbides; b) EDS line scan profile from the line in a); c) STEM image of a coarse carbide; d) EDS line scan profile from the line in c).

CONCLUDING COMMENTS

The oxidised sample of experimental 9Cr-1Mo ferritic steel examined here illustrates that both FIB and HS-AFM imaging can be used to observe the carbide precipitates. HS-AFM is capable of imaging small precipitates under 10 nm in size within a region of $4.5 \times 4.5 \mu\text{m}$ at high resolution of 4.5 nm and many such images may be stitched together to cover large areas. Both the FIB and HS-AFM images confirm that the fine needle carbides are found only intragranularly while the coarse carbide precipitates are at grain boundaries and within grains. The area percentage of fine needle precipitates decreases with depth from the metal/oxide interface. The plots in Figure 3a display a high area fraction at the edge and low in the centre of the fin demonstrating that the process of carburisation is effected by carbon diffusing from the surfaces of the fin. In addition, Figure 3b provides evidence of the carbide distribution from the fin tip, which is in accordance with the HS-AFM intensity map shown in Figure 1c. The explanation of a lower area fraction on the edge of fin in HS-AFM plot compared with FIB results may be due to differences in areas sampled, image processing or depletion of Cr in the process of oxidation. These effects will be the subject of further study. The similar trend obtained for carbide area fraction distribution from FIB and HS-AFM results and the finer spatial detail displayed by HS-AFM confirms the value of the technique for carburisation characterisation.

STEM / EDS results show that carbides with different morphologies are of different types based on the elemental distribution. The fine needle carbides are comprised mainly of Cr, Mo and C while the coarse carbides are composed of Fe, Cr, Mo and C. An exposed steel sample with a similar carbide

precipitate morphology and distribution (the needles were larger) examined with X-ray diffraction (XRD) indicated that the coarse precipitates were $M_{23}C_6$ and the large needle precipitates M_7C_3 ^[15]. As shown by equation 2, the deposited carbon reacts with the parent metal elements Fe, Cr and Mo to form carbide precipitates. For this non-equilibrium diffusion process, Cr would be consumed resulting in less protection for the parent ferrite which may eventually lead to breakaway oxidation.

ACKNOWLEDGEMENTS

Financial supports from EDF Energy Ltd, China Scholarship Council and Alumni Foundation are gratefully acknowledged. The views expressed are that of the authors and not of EDF Energy Ltd. Payton and Picco would like to thank the Royal Academy of Engineering for their support of the HS-AFM.

REFERENCES

- ¹ Ukai S., Harada M., Okada H., Inoue M., Nomura S., Shikakura S., Nishida T., Fujiwara M. and Asabe K. (1993). "Tube manufacturing and mechanical properties of oxide dispersion strengthened ferritic steel," *Journal of Nuclear Materials*, 204 74-80.
- ² Taylor J.W. (1983). "AGR Boiler Materials Selection Considerations," *Gas-cooled Reactors Today* BNES, London, 328 183-190.
- ³ Gibbs G.B. and Popple L.A. (1982). "Oxidation of Structural Steels in CO₂ Cooled Reactors," *Nuclear Energy*, 21 51-55.
- ⁴ Khanna A. S., Rodriguez P. and Gnanamoorthy J. B. (1986). "Oxidation Kinetics, Breakaway Oxidation, and Inversion Phenomenon in 9Cr-1Mo Steels," *Oxidation of Metals*, 26 171-200
- ⁵ Natesan K., Li M., Chopra O.K. and Majumdar S. (2009) "Sodium effects on mechanical performance and consideration in high temperature structural design for advanced reactors," *Journal of Nuclear Materials*, 392 243-248.
- ⁶ Robertson J. (1990) "The Mechanism of Carbon Deposition during the Breakaway Oxidation of Steels in Carbon Dioxide-model of Duplex Layer," *Catalysis Today*, 7 267-276.
- ⁷ Martinelli L., Desgranges C., Rouillard F., Ginestar K., Tabarant M. and Rousseau K. (2015). "Comparative Oxidation Behaviour of Fe-9Cr Steel in CO₂ and H₂O at 550 °C: Detailed Analysis of the Inner Oxide Layer," *Corrosion Science*, 100 253-266.
- ⁸ Newcomb S.B., Stobbs W.M. and Metcalfe E. (1986). "A Microstructural Study of the Oxidation of Fe-Ni-Cr Alloys II. 'Non-Protective' Oxide Growth," *Philosophical Transactions of the Royal Society of London. Series A, Mathematical and Physical Sciences*, 319 219-247.
- ⁹ Gheno T., Monceau D., Zhang J.Q. and Young D.J. (2011). "Carburisation of Ferritic Fe-Cr alloys by low carbon activity gases," *Corrosion Science*, 53 2767-2777.
- ¹⁰ Andren H. O., Cai G. J. and Svensson L. E. (1995). "Microstructure of heat resistant chromium steel weld metals," *Applied Surface Science*, 87/88 200-206.
- ¹¹ Rouillard F., Moine G., Tabarant M. and Ruiz J. C. (2012). "Corrosion of 9Cr Steel in CO₂ at Intermediate Temperature II: Mechanism of Carburization," *Oxidation of Metals*, 77 57-70.
- ¹² Vijayalakshmi M., Saroja S., Paul V. T., Mythili R., and Raghunathan V. S. (1999). "Microstructural Zones in the Primary Solidification Structure of Weldment of 9Cr-1Mo Steel," *Metallurgical and Materials Transaction A*, 30A 161-174.
- ¹³ Warren A., Martinez-Ubeda A., Payton O., Picco L. and Scott T. (2016). "Preparation of stainless steels surfaces for scanning probe microscopy techniques," *Microscopy Today*, 24. doi:10.1017/S1551929516000341.
- ¹⁴ Payton O. D., Picco L. and Scott T. B. (2016). "High-speed atomic force microscopy for materials science," *International Materials Reviews*, 61 473-493. doi:10.1080/09506608.2016.1156301.
- ¹⁵ Liu C., Heard P. J. and Flewitt P. E. J. (2018). to be published